

Novel Mn–Cu-Containing CeO₂ Nanopolyhedra for the Oxidation of CO and Diesel Soot: Effect of Dopants on the Nanostructure and Catalytic Activity

Melodj Dosa^{1,2} · Marco Piumetti^{1,2} · Samir Bensaid^{1,2} · Tahrizi Andana^{1,2} · Chiara Novara^{1,2} · Fabrizio Giorgis^{1,2} · Debora Fino^{1,2} · Nunzio Russo^{1,2}

Received: 10 August 2017 / Accepted: 5 October 2017 / Published online: 29 October 2017
© Springer Science+Business Media, LLC 2017

Abstract Ceria-based catalysts doped with manganese and copper were obtained via the hydrothermal synthesis. Four systems were synthesized: CeO₂ (pure ceria), Ce_{0.95}Mn_{0.05} (Mn/Ce at. ratio = 1/19), Ce_{0.95}Cu_{0.05} (Cu/Ce at. ratio = 1/19) and Ce_{0.95}Mn_{0.025}Cu_{0.025} (Mn/Cu/Ce at. ratio = 1/1/38). The catalytic activity of the prepared materials was tested for the CO and soot oxidations. Complementary techniques (XRD, N₂ physisorption at –196 °C, FESEM, XPS, Raman spectroscopy, CO-TPR and Soot-TPR) were performed to investigate their physico-chemical properties. The samples were characterized by nanocubes, in the case of CeO₂, and by nanopolyhedra for binary (Ce_{0.95}Mn_{0.05} and Ce_{0.95}Cu_{0.05}) and ternary oxides (Ce_{0.95}Mn_{0.025}Cu_{0.025}). The

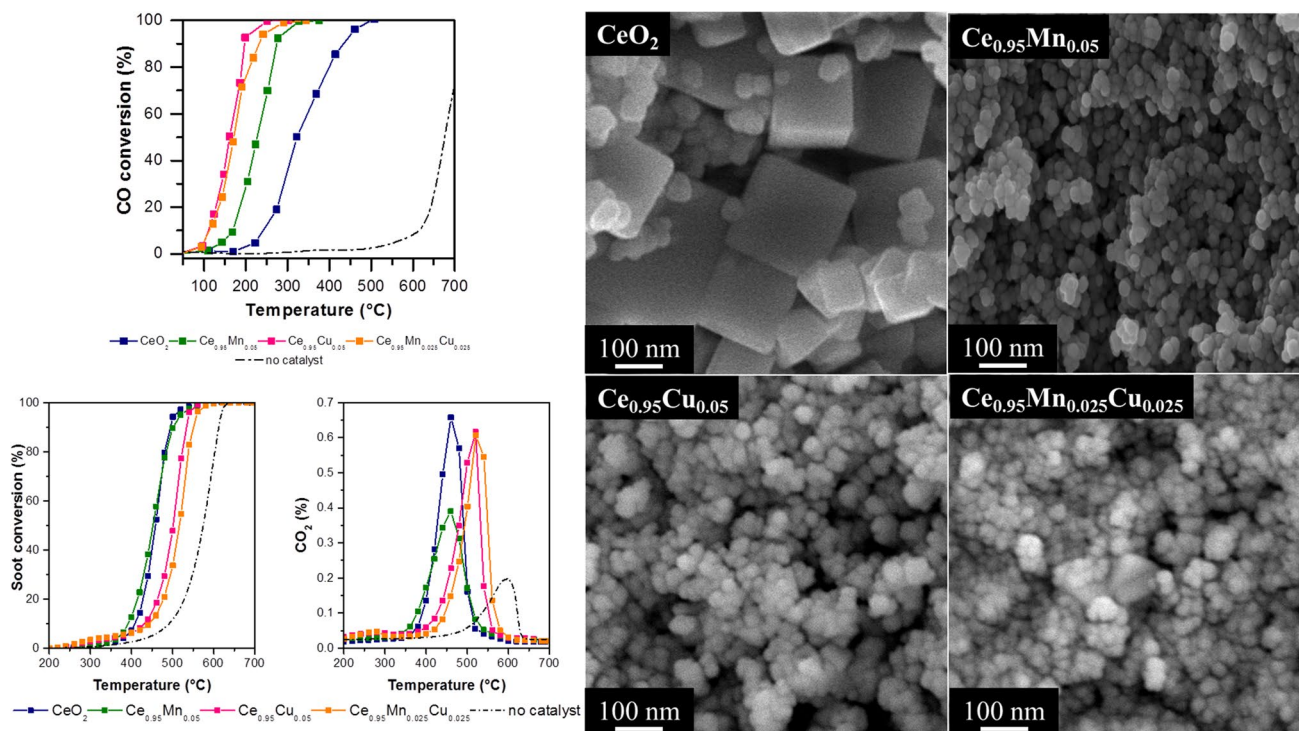
CO-TPR analysis has confirmed that the reducibility follows the order: CeO₂ < Ce_{0.95}Mn_{0.05} < Ce_{0.95}Mn_{0.025}Cu_{0.025} < Ce_{0.95}Cu_{0.05}. A similar trend appears for the surface defective sites (Raman spectroscopy). These findings suggest the beneficial role of dopants in improving the structural defects and the surface reducibility of ceria. Both properties promote the CO oxidation activity. In fact, the Ce_{0.95}Cu_{0.05} was the most effective catalyst for the CO oxidation. The Ce_{0.95}Mn_{0.05} sample exhibited the best performance in soot oxidation. The following order was achieved: Ce_{0.95}Mn_{0.025}Cu_{0.025} < Ce_{0.95}Cu_{0.05} < CeO₂ ≈ Ce_{0.95}Mn_{0.05}, in agreement with the reduction profiles obtained by the Soot-TPR above 400 °C.

✉ Marco Piumetti
marco.piumetti@polito.it

¹ Politecnico di Torino, Corso duca degli Abruzzi, 24,
10128 Turin, Italy

² Department of Applied Science and Technology, Politecnico
di Torino, Corso Duca degli Abruzzi 24, 10129 Turin, Italy

Graphical Abstract



Keywords Nanostructured ceria · CO oxidation · Soot oxidation · Manganese–ceria · Copper–ceria

1 Introduction

During the last few decades, rare earth materials have been widely investigated in the field of heterogeneous catalysis to improve the reactivity, stability and electron conductivity of solid catalysts. In the field of automotive catalysis, in particular, ceria-based catalysts have been the most frequently studied materials [1–7]. The extensive investigations into ceria hark back to its early application in the three-way catalytic converter [8, 9], a catalytic technology that benefits from the unique ceria redox properties. In fact, CeO₂-based systems participate in the oxidation reaction via redox cycles [10] and provide a high oxygen storage capacity (OSC) [4, 11].

Over the years, several studies have shown that ceria nanoparticles may exhibit different morphologies and structures [2, 7, 12–14]. In several previous works, well-defined ceria nanocubes and nanorods have been successfully prepared via a hydrothermal synthesis under various aging temperatures [2, 15, 16]. The hydrothermal synthesis, indeed, allows to obtain ceria-based nanoparticles with different morphologies, structural and textural properties, depending on the

synthesis conditions (i.e. aging temperature, molarity of the solution, ...) [2, 17].

The transmission electron microscopy has shown that a single CeO₂-based nanocube consisted of six well-defined (100)-type crystalline planes, while a CeO₂ nanorod was predominantly constituted of (110)-type planes [2, 17]. In terms of catalytic activity, both the nanocubes and nanorods have been found to outperform the “conventional” polycrystalline CeO₂ (obtained by the solution combustion synthesis) for both the CO oxidation and soot combustion reactions [2, 6, 7, 17, 18]. This finding is most likely due to the lower energy for the formation of oxygen vacancies and higher oxygen reactivity with the low index facets. In fact, the oxygen reactivity among low-index facets is believed to follow the order: (100) > (110) > (111), while the energy for the formation of vacancies is (110) < (100) < (111) [19, 20]. Finally, (111)-type planes were found to be more abundant for polycrystalline ceria.

As is known, the physico-chemical properties of ceria can be modified by introducing foreign metals (e.g., Zr, Pr, Cu, etc.) into the ceria lattice. Depending on the nature of the metal, these additional elements may lead to more structural defects in the ceria framework, higher OSC and better thermal stability [18, 21–25]. Among the frequently investigated foreign metals, Cu and Mn are of particular interest. Specifically, CuO–CeO₂ systems have been particularly effective towards both the CO and soot oxidation reactions

[23, 26–29]. A synergistic effect was ascribed to the coupled redox cycles $\text{Ce}^{3+}|\text{Ce}^{4+}$ and $\text{Cu}^{2+}|\text{Cu}^+$ ions, the enhanced number of defective sites (e.g., oxygen vacancies) and the higher surface reducibility [26, 30, 31]. In our previous work, a copper-ceria mixed oxide sample (the $\text{Ce}_{0.95}\text{Cu}_{0.05}$ sample prepared through the solution combustion synthesis, Cu/Ce atomic ratio = 1/19) was found to be the best combination for the soot combustion reaction [26]. Likewise, the soot oxidation, NO oxidation and CO oxidation carried out over $\text{CeO}_2\text{--MnO}_x$ catalysts also benefit from the coupled redox cycles $\text{Mn}_2\text{O}_3|\text{MnO}_2$ and $\text{CeO}_2|\text{Ce}_2\text{O}_3$ [32–34]. On the other hand, little attention has been paid to the ternary $\text{CeO}_2\text{--MnO}_x\text{--CuO}_x$ systems, which turn out to give higher catalytic activity towards the CO oxidation and toluene oxidation than the conventional binary oxides [35–37].

The present work aims to study a set of ceria-based materials doped with copper and manganese. All the catalysts were synthesised via the hydrothermal synthesis. Four systems were investigated: CeO_2 (pure ceria), $\text{Ce}_{0.95}\text{Mn}_{0.05}$ (Mn/Ce atomic ratio = 1/19), $\text{Ce}_{0.95}\text{Cu}_{0.05}$ (Cu/Ce atomic ratio = 1/19) and $\text{Ce}_{0.95}\text{Mn}_{0.025}\text{Cu}_{0.025}$ (Mn/Cu/Ce atomic ratio = 1/1/38). CO and soot oxidations were used as probe reactions. Complementary characterisations, such as the powder XRD, N_2 physisorption at -196°C , FESEM, XPS, micro-Raman spectroscopy, CO-TPR and Soot-TPR analysis were performed to investigate the physico-chemical properties of the prepared catalysts.

2 Experimental

2.1 Catalyst Preparation

Four ceria-based samples were prepared by the hydrothermal synthesis: CeO_2 , $\text{Ce}_{0.95}\text{Mn}_{0.05}$ (Mn/Ce atomic ratio = 1/19), $\text{Ce}_{0.95}\text{Cu}_{0.05}$ (Cu/Ce atomic ratio = 1/19) and $\text{Ce}_{0.95}\text{Mn}_{0.025}\text{Cu}_{0.025}$ (Mn/Cu/Ce atomic ratio = 1/1/38). Subscripts indicate the atomic fractions of the metal cations. Briefly, stoichiometric quantities of $\text{Ce}(\text{NO}_3)_3 \cdot 6\text{H}_2\text{O}$ (Sigma-Aldrich) and $\text{Cu}(\text{NO}_3)_2 \cdot 5\text{H}_2\text{O}$ (Sigma-Aldrich) and/or $\text{Mn}(\text{NO}_3)_2 \cdot 4\text{H}_2\text{O}$ (Sigma-Aldrich) were dissolved in 10 ml of deionised water (*solution A*). Then, 48 g of NaOH were dissolved in 70 ml of deionised water (*solution B*). The salt precursor solution (*A*) was then added drop by drop into the hydroxide solution (*B*). The final mixture (*A + B*) was stirred at room temperature for 1 h. The final slurry was then poured into a 150-ml Teflon liner, that was later secured in an autoclave. The autoclave was heated in an oven for an aging treatment at 180°C for 24 h. The resulted precipitate was washed with ethanol and deionised water and then dried overnight at 60°C . Finally, the dry powder was calcined at 550°C for 4 h.

2.2 Catalyst Characterization

Powder X-ray diffractograms of the catalysts were recorded on an X'Pert Philips PW3040 diffractometer using Cu $\text{K}\alpha$ radiation (2θ range = $20^\circ\text{--}70^\circ$; step = $0.05^\circ 2\theta$; time per step = 0.2 s). The diffraction peaks were indexed according to the Powder Data File database (PDF 2000, International Centre of Diffraction Data, Pennsylvania). Crystallite size [D_c , (nm)] was estimated by the Scherrer's equation, $D_c = 0.9 \lambda / (\beta \cos \theta)$, where 0.9 is the shape factor for sphere, λ is the Cu $\text{K}\alpha$ wavelength (nm), β is the full-width at half maximum [FWHM (rad)] and θ is the Bragg angle (rad). Prior to the calculation, the FWHM data were corrected with respect to those of lanthanum hexaboride (instrument calibration standard).

BET specific surface area (S_{BET}), total pore volume (V_p) and pore diameter (D_p) of the catalysts were measured via the N_2 physisorption at -196°C (Micrometrics ASAP 2020). Prior to the analysis, the catalysts were outgassed at 200°C for 2 h.

Catalyst morphology was analysed via a field emission scanning electron microscope (FESEM Zeiss MERLIN, Gemini-II column).

Raman measurements were carried out on a Renishaw InVia Reflex micro-Raman spectrometer with laser excitation at 514.5 nm in backscattering light collection. The O_v/F_{2g} value, representative of oxygen vacancies density, was calculated as the ratio between the integrated areas of the oxygen vacancies related Raman bands (O_v) and the main vibrational band related to the ceria matrix (F_{2g}) obtained by averaging the spectra recorded on three different areas of the sample.

The oxidation states for the elements of interest (namely, Ce, Mn, Cu and O) were investigated via X-ray photoelectron spectroscopy, performed in a PHI Versa probe apparatus using a band-pass energy of 187.85 eV, a 45° take-off angle and 100 μm diameter X-ray spot size.

CO-TPR and Soot-TPR measurements were carried out for evaluating the reducibility of the prepared catalysts. CO-TPR is basically an anaerobic catalytic CO oxidation, that is the reaction whose oxygen source solely comes from the catalyst surface. The reduction was performed in a U-tube reactor, whose fixed catalytic bed contains 45 mg of catalyst and 150 mg of silica. The analysis began with a catalyst pretreatment with 200 ml min^{-1} of N_2 at 100°C for 1 h. Then, the reducing gas (2000 ppm-vol of CO in N_2) was introduced into the reactor at a rate of 200 ml min^{-1} . The ramp heating by a PID-controlled electric furnace (rate = $10^\circ\text{C min}^{-1}$) started upon the gas introduction. The test ended when the reactor temperature reached 700°C .

Similarly, Soot-TPR was additionally carried out to evaluate catalyst reduction in the presence of soot. A bed mixture containing 5 mg of commercial soot (Printex-U), 45 mg of

powder catalyst and 150 mg of silica was prepared in “tight contact” and put inside the same fixed-bed reactor.

2.3 Catalyst Performance

A typical temperature-programmed combustion (TPC) setup was used during the test of catalytic performances. The apparatus was comprised of a quartz U-tube fixed-bed reactor (ID=4 mm, OD=6 mm), a PID-controlled electric furnace, a K-type thermocouple placed in such a way that the sensor tip was as close as possible to the reactor bed. Temperatures corresponding to 10, 50, 90% conversion (denoted as $T_{10\%}$, $T_{50\%}$, $T_{90\%}$, respectively) were taken as indices of the activity of the tested catalysts. Evolution of CO and CO₂ was monitored by a non-dispersive infrared analyser (ABB Uras 14). CO and soot oxidations were used as probe reactions.

2.3.1 CO Oxidation Reaction

The reactor bed contained 100 mg of catalyst. The reactor was initially pre-treated by air (flow rate = 50 ml min⁻¹) for 30 min at 150 °C. Then, the reactor was naturally cooled down until 50 °C while the airflow was still maintained. The test started with gas introduction (1000 ppm-vol of CO and 10%-vol O₂ in N₂) into the reactor at a rate of 50 ml min⁻¹ at 50 °C. The reactor temperature was then increased manually by 50 °C. After each increment, the reactor was kept isothermal for a certain period to allow better concentration stabilisation, possibly affected by adsorption–desorption phenomena. The test ended when 100% of CO conversion was reached.

2.3.2 Soot Oxidation Reaction (Under “Tight” Contact Condition)

The reactor bed contained an intimate mixture of 5 mg of model soot (Printex-U by Degussa), 45 mg of powdered catalyst and 150 mg of silica, made in a ball-miller (Giuliani Tecnologie Srl) operated at 290 rpm for 15 min. The latter condition guarantees a “tight” contact between the catalyst and soot. This method maximizes the number of contact points and, although it is less representative of the real contact conditions that occur in a catalytic trap, it is able to discriminate better the role of catalyst morphology. The reactor was initially pre-treated by air (flow rate = 100 ml min⁻¹) for 30 min at 100 °C. The test began with gas introduction (50%-vol air and 50%-vol N₂) into the reactor at a rate of 100 ml min⁻¹. The reactor temperature was then increased from 100 to 700 °C with a programmed heating rate of 5 °C min⁻¹.

3 Results and Discussion

3.1 Textural Properties

The powder X-ray diffractograms of the prepared catalysts are summarised in Fig. 1. As a whole, they exhibit the typical pattern of the fluorite structure of ceria, that is known to be characterized by the peaks related to the (111), (200), (220), (311) and (222) planes [2, 17, 18]. The inset of Fig. 1 shows the magnification of the (111) peak in the 2θ range (from 28° to 29°). The inset shows that the peaks of the mixed oxide samples are shifted to higher 2θ values. This is most likely due to ceria lattice shrinkage, as the ionic radii of Ce [r_{ion} of Ce³⁺/Ce⁴⁺ (CN=6) is 1.01/0.87 Å] are generally higher than those of Mn and Cu [r_{ion} of Mn³⁺/Mn⁴⁺ (CN=6) is 0.58/0.53 Å and r_{ion} of Cu⁺/Cu²⁺ (CN=6) is 0.77/0.73 Å] [38]. The Ce_{0.95}Mn_{0.05} sample shows the biggest peak shift (ca. 0.25°) as Mn has the smallest ionic radii among the investigated metal cations. As expected, lower shifts are encountered in the diffractograms of Ce_{0.95}Cu_{0.05} and Ce_{0.95}Mn_{0.025}Cu_{0.025} samples (0.07° and 0.09°, respectively). In Fig. 1 the intensity of the (200) and (220) peaks, relative to the (111) peak, may shed light upon the relative abundance of low-index planes. Table 1 summarises these two ratios, denoted as (200)/(111) and (220)/(111), respectively.

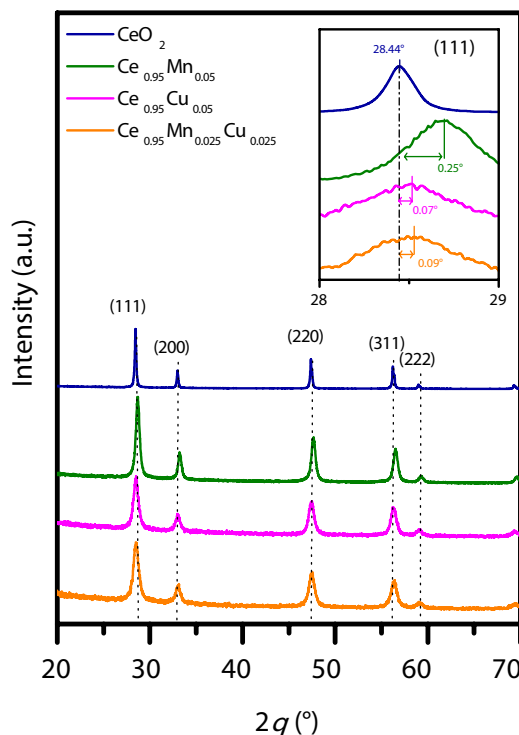


Fig. 1 X-ray diffractograms for the prepared samples. (Inset) Magnification of the (111) peak for the 2θ shift observation

Table 1 Textural properties of the prepared catalysts obtained from X-ray diffraction and N₂ physisorption

Catalysts	(200)/(111) ^a	(220)/(111) ^a	D_c^b (nm)	S_{BET}^c (m ² g ⁻¹)	V_p^d (cm ³ g ⁻¹)	D_p^e (nm)
CeO ₂	0.30	0.51	135	9	0.03	12
Ce _{0.95} Mn _{0.05}	0.32	0.50	39	33	0.18	21
Ce _{0.95} Cu _{0.05}	0.35	0.68	34	46	0.16	14
Ce _{0.95} Mn _{0.025} Cu _{0.025}	0.33	0.59	23	52	0.15	11

^aXRD peak intensity ratio^bCrystallite size estimated by Scherrer's equation^cSpecific surface area calculated by BET method^dTotal pore volume^ePore diameter

As a whole, the addition of the Cu and Mn cations into the ceria framework leads to more abundant low-index planes, particularly in the presence of Cu species. Specifically, the Ce_{0.95}Cu_{0.05} sample has the highest (220)/(111) and (200)/(111) ratios.

Figure 1 shows that the peaks of CeO₂ and Ce_{0.95}Mn_{0.05} samples appear sharper and narrower than those of Ce_{0.95}Cu_{0.05} and Ce_{0.95}Mn_{0.025}Cu_{0.025}, thus suggesting bigger crystallite sizes. Then, the Scherrer's equation was used to estimate the crystallite size (D_c), whose calculated values for all catalysts are also summarised in Table 1. The CeO₂ sample exhibits larger D_c (ca. 135 nm) than the other mixed oxide samples (in the range of 23 to 39 nm). Interestingly, the Cu-containing catalysts have the smallest D_c (23–34 nm), thus suggesting a significant change in the CeO₂ lattice. Results from N₂ physisorption are also summarised in Table 1. The BET specific surface area (S_{BET}) of pure CeO₂ is the lowest in the series (9 m² g⁻¹). On the other hand, the surface areas of mixed oxide samples are generally higher than the one of CeO₂. Interestingly, the Cu-containing catalysts (including the ternary oxide) have the surface area almost five times higher than that of CeO₂. This suggests one more time the contribution of Cu doping to the modification of the microstructure. As previously suggested from XRD results, Cu doping leads to smaller crystallite size. The decrease in crystallite size may increase the number of interparticle voids in the catalyst framework, and so higher surface area can be observed.

The total pore volume of the catalysts (V_p) also follows the trend of surface area. Despite the high variability in S_{BET} , the average pore diameter (D_p) seems comparable among the catalysts (in the range of 11–21 nm).

Figure 2 shows the FESEM micrographs for the prepared catalysts. The CeO₂ sample, as previously reported in the literature, exhibits a well-defined nanocubic morphology rich in (100)-type facets [2, 17]. The average size of the cubes ranges from 100 to 300 nm. On the other hand, the cubic structure is vanished when copper and manganese are introduced into ceria lattice. Both the Ce_{0.95}Cu_{0.05} and Ce_{0.95}Mn_{0.05} samples are comprised of small polyhedra

(between 20 and 40 nm), with abundant low-index facets [7, 16, 21]. Similarly, the ternary sample exhibits clusters of small nanoparticles, in agreement with the XRD data (*vide supra*).

3.2 Surface Oxidation States and Defective Sites

Surface oxygen species of the prepared samples were analysed via the deconvoluted O 1s X-ray photoelectron spectra (Fig. 3a). In general, two major species can be distinguished:

- the so-called “O_β” species or commonly known as lattice oxygen species, marked by an intense peak at lower binding energy (BE) values (528.8–529.1 eV) [39, 40]
- the surface capping oxygen species (the “O_α”) that appears at higher BE values (531.2–531.6 eV). The species can be in the form of hydroxyls (OH⁻), carbonates (CO₃²⁻) and/or other anions, such as peroxy (O₂²⁻) and superoxy species (O₂⁻) [2, 40, 41]

Table 2 summarises the relative abundances of these two oxygen species for the prepared catalysts. The abundance of O_α in the binary oxide samples appears similar to that for the CeO₂ sample. However, when the three cations exist in the catalysts (ternary oxide) the O_α abundance increases. Such a phenomenon has also been observed for the Ce–Pr–Zr ternary oxides [42]. A richer population of O_α species on the catalyst surface may foster oxygen spillover coming from bulk dioxygen to the surface of ceria as it may enhance the electron mobility on the surface. It is widely understood that the spillover mechanism requires a dissociative adsorption of molecular oxygen step, during which electron transfers take place from metal sites to the antibonding π -orbital of the oxygen molecule until cleavage of the O–O bond is reached. This mechanism can be expressed as follows [43, 44]:

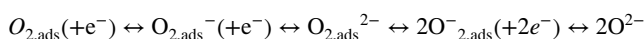


Figure 3b shows the deconvoluted Ce 3d spectra of the prepared catalysts. By default, eight sub-peaks have been deconvoluted in the spectra: the ν quadruplets in the Ce 3d_{5/2}

Fig. 2 FESEM micrographs for the prepared samples

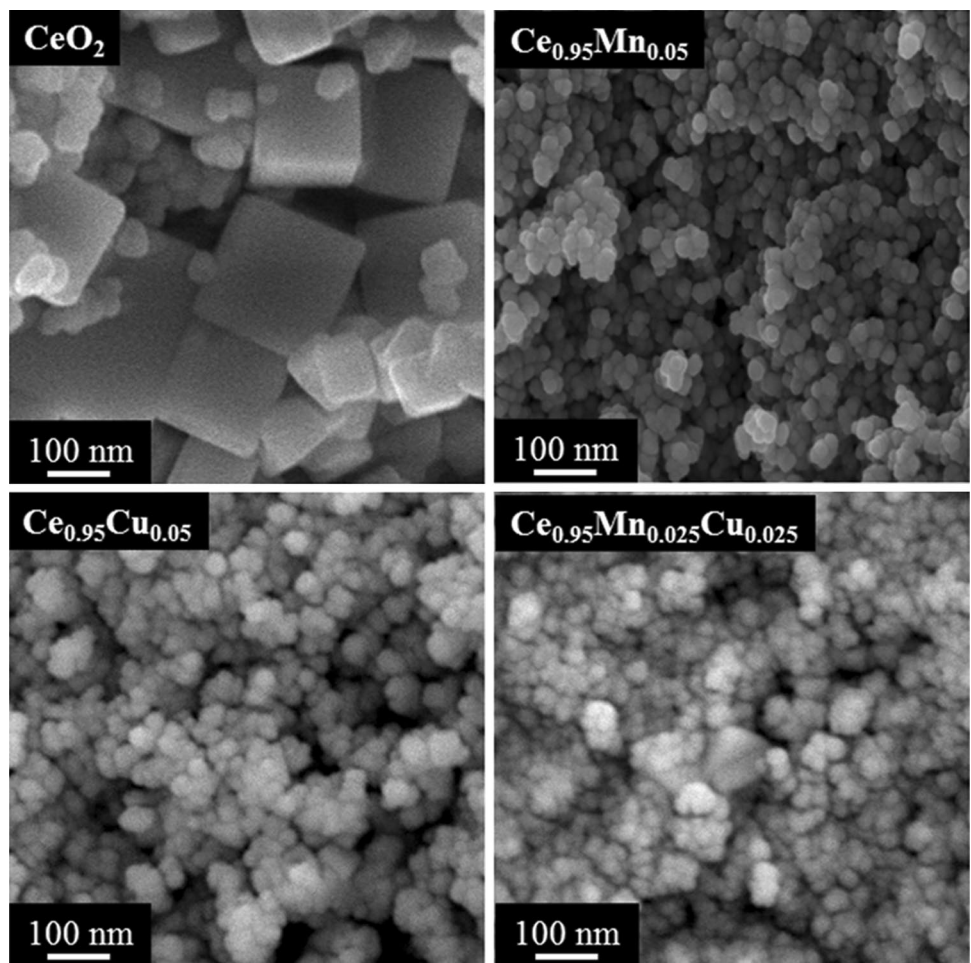


Fig. 3 Deconvoluted X-ray photoelectron spectra of *a* CeO₂, *b* Ce_{0.95}Mn_{0.05}, *c* Ce_{0.95}Cu_{0.05} and *d* Ce_{0.95}Mn_{0.025}Cu_{0.025} in the **A** O 1s and **B** Ce 3d core levels

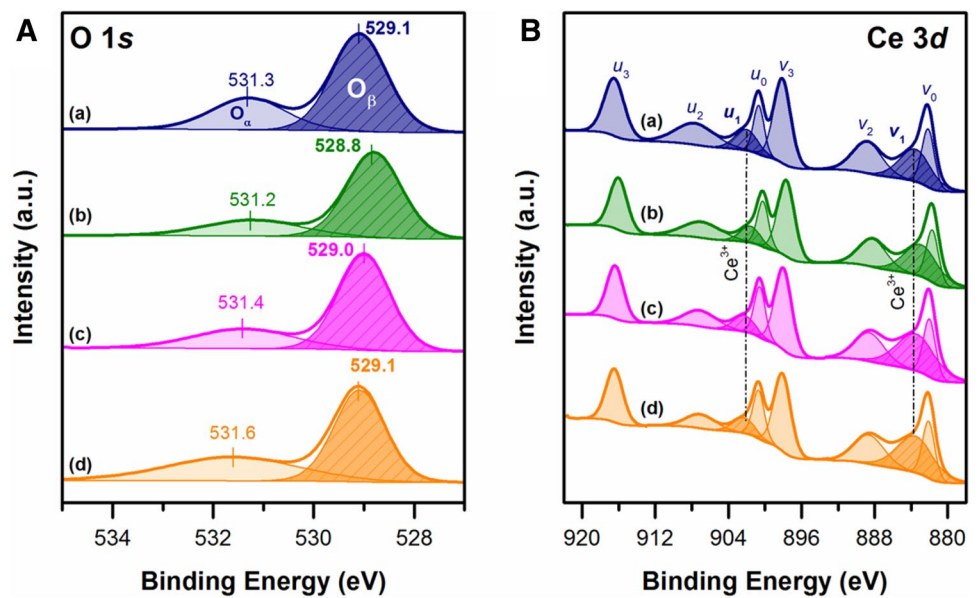


Table 2 Relative abundances of O_α , O_β and Ce^{3+} species (in atomic percentage) derived from deconvoluted XP spectra

Catalyst	O_α species		O_β species		[Ce^{3+}] (% at.)
	BE (eV)	[O_α] (% at.)	BE (eV)	[O_β] (% at.)	
CeO_2	531.3	31	529.1	69	21
$Ce_{0.95}Mn_{0.05}$	531.2	25	528.8	75	23
$Ce_{0.95}Cu_{0.05}$	531.4	29	529.0	71	27
$Ce_{0.95}Mn_{0.025}Cu_{0.025}$	531.6	40	529.1	60	26

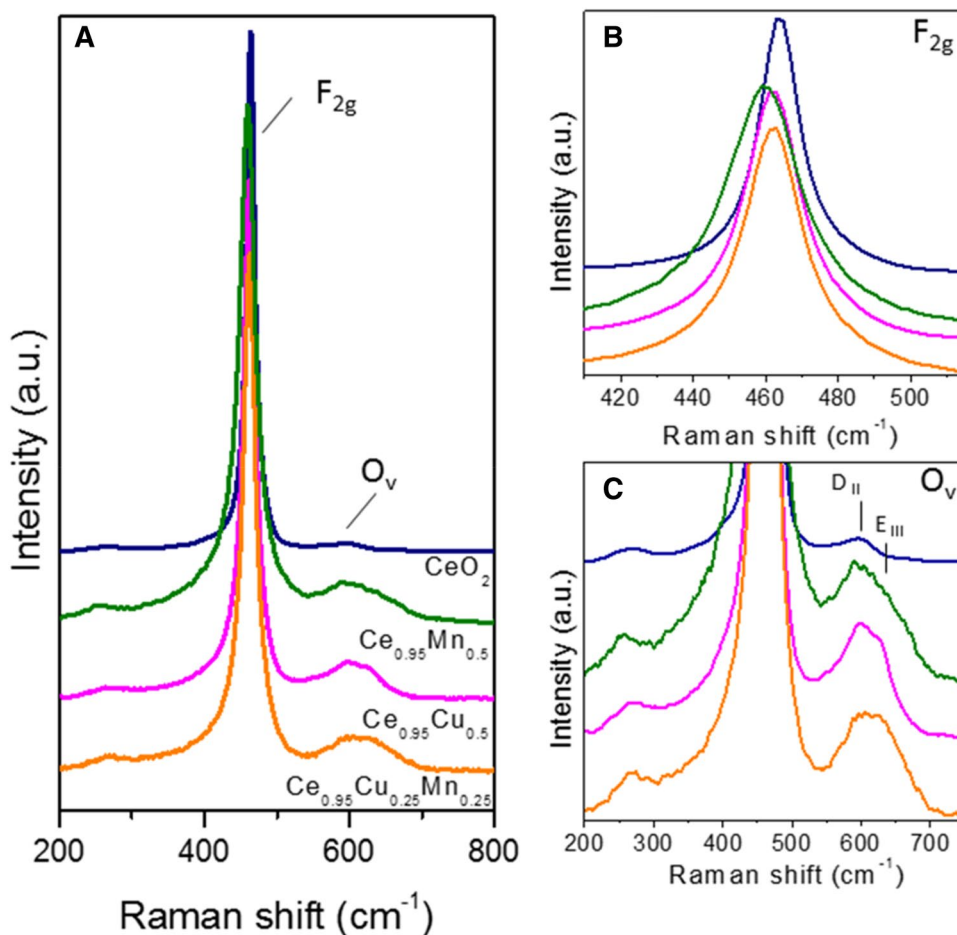
region and the u quadruplets in the $Ce\ 3d_{3/2}$ region. Two sub-peaks v_1 and u_1 (marked by areas with darker shades on the figure) are the unique markers for Ce^{3+} species while the rest of the sub-peaks are ascribed to Ce^{4+} species [39, 45, 46]. Table 2 also summarises the abundances of the Ce^{3+} species (in atomic %) relative to the Ce^{4+} species of the prepared catalysts. The $Ce_{0.95}Mn_{0.05}$ sample has a similar surface Ce^{3+} abundance with the CeO_2 sample, while the $Ce_{0.95}Cu_{0.05}$ sample has a higher abundance of Ce^{3+} species. This suggests that the Cu insertion in the CeO_2 framework promotes the creation of Ce^{3+} species.

For the sake of brevity, the Cu $2p$ and Mn $2p$ spectra of the doped catalysts are not shown. In fact, due to their low concentrations in the solid solutions (2.5 and 5.0 at.% for

ternary and binary oxides, respectively), the characteristic peaks are very low in intensity and hence hardly observable in the XPS spectra. Therefore, peak deconvolutions were not performed as they may lead to unreliable interpretations.

The Raman spectra of the four catalysts are reported in Fig. 4a. Indeed, Raman spectroscopy can provide additional insight into the influence of doping on the structural features of ceria and highlight the formation of new defective sites [47, 48]. All the spectra were normalised to the main Raman peak of ceria-based materials, the F_{2g} mode, ascribed to the symmetric vibration of the Ce–O bonds of the fluorite crystal unit [49]. The position of this peak is sensitive to the incorporation of the dopants as witnessed by its marked red-shift in the binary and ternary oxides (Fig. 4b). The displacement

Fig. 4 **a** Raman spectra of the prepared catalysts; **b** enlarged view of the F_{2g} peak; **c** enlarged view of the defect bands region



of the F_{2g} band centre towards lower Raman shifts is usually explained in terms of expanded lattice parameters due to the incorporation of bigger cations combined to an increased defectiveness and strain effects [48].

While the first phenomenon can be ruled out based on the ionic radius of the dopants and on the XRD measurements, both the increased content of oxygen vacancies and strains induced by the shrinkage of the unit cell are likely to contribute to the red shift. The higher strain due to the replacement of Ce⁴⁺ with the smallest cation in the Ce_{0.95}Mn_{0.05} sample is in agreement with the strongest shift observed for the F_{2g} mode. Together with the change in position, a broader linewidth is detected for the doped samples. An increased peak width may depend on a higher defectiveness [50], which can be assessed through the analysis of the spectral region between 500 and 650 cm⁻¹, where disorder-induced bands can be identified. A single peak located at 595.9 cm⁻¹ characterises the Raman pattern of pure ceria and, according to the work of Wu et al. [51] was previously assigned to oxygen vacancies part of a Frenkel anion pair. The defect band becomes broader and significantly more intense for the doped materials. Indeed, different defect sites can feature the ceria matrix. Usually, they are distinguished in intrinsic and extrinsic defects. The former consist of (i) oxygen vacancies due to the presence of reduced Ce³⁺ cations (D_I Raman peak around 550–560 cm⁻¹) [51] and (ii) Frenkel type anion defects (D_{II}, 595–600 cm⁻¹) [52]. Instead, extrinsic defects can be introduced by the incorporation of doping elements. In detail, oxygen vacancies created to compensate the lower positive charge of trivalent dopant cations are believed to provide vibrational bands close to the D_I species (E_I) [53], while the presence of substitutional cations in eightfold coordination has been also suggested to produce a defect-related band around 600 cm⁻¹ (E_{II}) [54]. Moreover, the dopants incorporation can furtherly promote the formation of intrinsic defects in ceria. A closer inspection of the defect spectral range, shown in Fig. 4c, allows to resolve a new component at higher Raman shifts for the Cu and Mn containing catalysts, in addition to the Frenkel defects mode around 595 cm⁻¹. According to the deconvolution of the broad defect band, such peak is found at 628 cm⁻¹ for the Ce_{0.95}Cu_{0.05} sample, 637 cm⁻¹ for the Ce_{0.95}Mn_{0.05} sample and at an intermediate Raman shift value for the ternary oxide. The dependence of its spectral position on the dopant type suggests its classification as an extrinsic defect band (E_{III}). It should be noted, that besides this new component, also the peak at 595 cm⁻¹ grows in intensity in presence of dopants, contributing to the overall increase in the intensity of the oxygen vacancies related band compared to pure ceria. In particular, the oxygen vacancy content for each catalyst was estimated by means of the calculated ratio between the total integrated area of the D_{II} and E_{III} bands and the one of the F_{2g} peak (O_v/F_{2g}). Such values are summarised

Table 3 Calculated O_v/F_{2g} ratios for the different catalysts

Catalyst	O _v /F _{2g}
CeO ₂	0.022
Ce _{0.95} Mn _{0.05}	0.183
Ce _{0.95} Cu _{0.05}	0.240
Ce _{0.95} Mn _{0.025} Cu _{0.025}	0.239

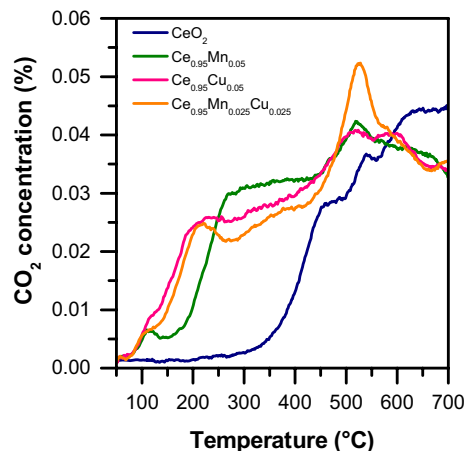


Fig. 5 CO-TPR profiles: CO₂ evolution as a function of temperature

in Table 3, from which it can be inferred that the Cu-containing catalysts are featured by the highest O_v/F_{2g} ratios. This could be ascribed to an increased defect density, taking into account that Ce_{0.95}Cu_{0.05} and Ce_{0.95}Mn_{0.025}Cu_{0.025} are characterised by the highest specific surface area.

3.3 Reducibility

The employment of carbon monoxide as the reducing agent in a TPR analysis benefits from its direct correlation with CO oxidation, one of the probe catalytic reactions investigated in the present work. Under anaerobic conditions, CO consumes the surface and bulk oxygens that come from the solid catalyst. The oxygen species are recognisable from the temperatures at which their corresponding CO₂ production peaks occur.

Figure 5 shows the evolution of CO₂ (%) as a function of temperature during the CO-TPR analysis. It can be observed that at low temperatures (from 100 to 200 °C), the reduction lights off over doped-ceria catalysts. The Cu-containing catalysts (Ce_{0.95}Cu_{0.05} and Ce_{0.95}Mn_{0.025}Cu_{0.025}) demonstrate the earliest oxygen consumption by CO, followed by the Ce_{0.95}Mn_{0.05} catalyst. The low-temperature reduction peak is most likely due to the weakening of Ce–O bonds near the Ce-dopant (Cu/Mn) interface on the surface. On the other hand, in the previous study with ceria-praseodymia catalysts, the reduction-peak occurred at higher temperatures

(ca. 300 °C) [18]. This suggests that Mn/Cu perturbs the structure of ceria more predominantly on the surface than in the lattice, while the opposite has been observed for ceria-praseodymia catalysts.

To better quantify the reducibility at low temperature, the specific reaction rate for the CO oxidation under anaerobic conditions (r_{CO}) has been used. The latter can be defined as the rate of CO conversion normalised with respect to specific surface area of the catalyst at a certain temperature ($\text{mmol}_{\text{CO}} \text{m}^{-2} \text{h}^{-1}$). Table 4 summarises the r_{CO} values at 140 °C for the prepared catalysts. While r_{CO} is the lowest for the ceria sample ($5.11 \text{ mmol}_{\text{CO}} \text{m}^{-2} \text{h}^{-1}$), the metal doped-ceria catalysts somewhat demonstrate higher CO oxidation rates. In fact, the $\text{Ce}_{0.95}\text{Mn}_{0.05}$ sample has a similar rate of the $\text{Ce}_{0.95}\text{Mn}_{0.025}\text{Cu}_{0.025}$, despite the reduction lights off at a higher temperature. Conversely, the $\text{Ce}_{0.95}\text{Cu}_{0.05}$ sample exhibits higher CO oxidation rate ($22.70 \text{ mmol}_{\text{CO}} \text{m}^{-2} \text{h}^{-1}$) than the other mixed oxides. As a whole, the trend for the light-off temperatures among the catalysts follows this order:

$\text{CeO}_2 > \text{Ce}_{0.95}\text{Mn}_{0.05} > \text{Ce}_{0.95}\text{Mn}_{0.025}\text{Cu}_{0.025} > \text{Ce}_{0.95}\text{Cu}_{0.05}$, while the trend for the BET surface areas is the reverse

$\text{CeO}_2 < \text{Ce}_{0.95}\text{Mn}_{0.05} < \text{Ce}_{0.95}\text{Cu}_{0.05} < \text{Ce}_{0.95}\text{Mn}_{0.025}\text{Cu}_{0.025}$.

Interestingly, there is a direct correlation between the specific reaction rate of CO oxidation under anaerobic conditions and the abundance of structural defects on the catalyst surfaces, as evaluated by the Raman spectroscopy. Then, there is a broad activity region between ca. 200 and 450 °C, in which the reduction progressively increases for both the binary and ternary oxides. Conversely, the reduction for CeO_2 become significant at around 400 °C.

Above 400 °C, further reduction peaks can be observed for all the catalysts. The ternary oxide has the most intense peak centred at around 530 °C, thus confirming the beneficial role of both Cu and Mn species to reduce the ceria-based catalyst in this temperature range. On the other hand, similar reduction profiles can be observed for the binary oxide catalysts. As expected, the least intense reduction peak occurs for the CeO_2 . At high temperature (550–700 °C) all

catalysts show high activity, although the production of CO_2 seems constant. This phenomenon may be ascribed to the consumption of bulk oxygens from the ceria lattice [18, 42].

The reducibility of the catalysts was also examined by the Soot-TPR analysis, in which the samples were exposed to soot under the increasing temperature and in absence of gas-phase oxygen (anaerobic condition). This new characterization technique allows to evaluate the overall oxygen content in the solid, the reaction selectivity for CO/ CO_2 and the intrinsic activity of the catalyst [42].

As is known, the catalytic soot oxidation takes place by the oxygen of the solid catalyst according two key steps: (i) catalyst reduction at low temperature (in the range of 300 to 500 °C) that produces mainly CO_2 and (ii) high-temperature reduction (above 500 °C) in which CO formation occurs. These temperature ranges are comparable with the CO-TPR profiles of the catalysts (Fig. 6): the first reduction peak (CO_2 formation) appears between 200 and 400 °C followed by another reduction peak at higher temperature (Fig. 6a). On the other hand, the CO production occurred only above 600 °C, as shown in Fig. 6b (especially for the CeO_2 sample).

The reducibility of the catalysts by soot in the 200–400 °C temperature range increases as follows:

$\text{CeO}_2 \approx \text{Ce}_{0.95}\text{Mn}_{0.05} < \text{Ce}_{0.95}\text{Cu}_{0.05} < \text{Ce}_{0.95}\text{Mn}_{0.025}\text{Cu}_{0.025}$

On the other hand, above 400 °C a reverse trend can be observed

$\text{Ce}_{0.95}\text{Mn}_{0.025}\text{Cu}_{0.025} < \text{Ce}_{0.95}\text{Cu}_{0.05} < \text{CeO}_2 < \text{Ce}_{0.95}\text{Mn}_{0.05}$ thus suggesting that the $\text{Ce}_{0.95}\text{Mn}_{0.05}$ is the best soot oxidation catalyst under anaerobic conditions.

3.4 Catalytic Activity

3.4.1 CO Oxidation Reaction

The catalytic behavior towards the CO oxidation (%) was studied in the 50–600 °C temperature range. Figure 7 shows the CO conversion as a function of temperature over the

Table 4 Summary of the catalytic performances obtained from the tests with CO-TPR, CO-oxidation and soot oxidation

Catalyst	CO-TPR r_{CO} at 140 °C ^a	CO oxidation				Soot oxidation			
		$T_{10\%}$	$T_{50\%}$	$T_{90\%}$	r_{CO} at 140 °C ^b	$T_{10\%}$	$T_{50\%}$	$T_{90\%}$	r_{soot} at 320 °C ^c
CeO_2	5.11	241	324	432	1.30	409	455	494	0.58
$\text{Ce}_{0.95}\text{Mn}_{0.05}$	12.74	162	226	279	1.66	392	451	502	0.69
$\text{Ce}_{0.95}\text{Cu}_{0.05}$	22.20	110	162	198	6.76	430	503	533	0.77
$\text{Ce}_{0.95}\text{Mn}_{0.025}\text{Cu}_{0.025}$	13.39	118	172	236	4.59	441	516	552	0.70

^aSpecific reaction rate of anaerobic CO oxidation ($\text{mmol}_{\text{CO}} \text{m}^{-2} \text{h}^{-1}$)

^bSpecific reaction rate of aerobic CO oxidation ($\text{mmol}_{\text{CO}} \text{m}^{-2} \text{h}^{-1}$)

^cSpecific reaction rate of soot oxidation ($\text{mmol}_{\text{soot}} \text{g.cat}^{-1} \text{h}^{-1}$)

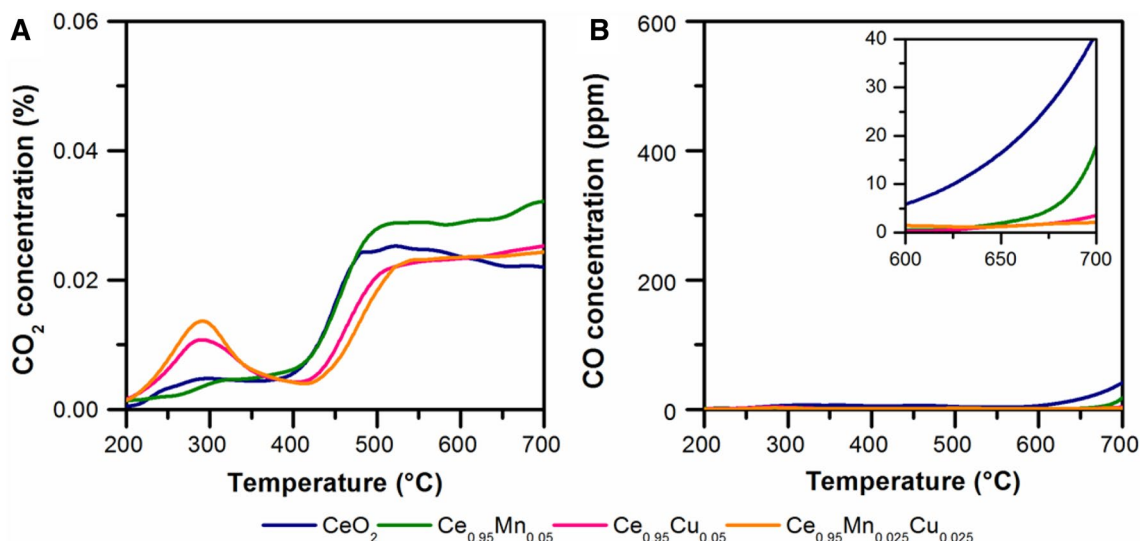


Fig. 6 Soot-TPR profiles: CO₂ (a) and CO concentrations (b) as a function of temperature

prepared catalysts, along with the uncatalysed CO oxidation (dash dot curve). Likewise, Table 4 summarises the catalytic performances, in terms of $T_{\text{conv}}(\%)$ (°C) and specific reaction rates (CO oxidation under aerobic conditions).

The former parameter ($T_{10\%}$, $T_{50\%}$ and $T_{90\%}$) is defined as the temperature at which the reaction reaches 10, 50 and 90% of CO conversion. The latter (r_{CO}) has been calculated at 140 °C, in agreement with the r_{CO} values derived from the CO-TPR analysis (anaerobic CO oxidation). As a whole, the CO oxidation activity (i.e. in terms of light-off temperature) correlates with the CO-TPR profiles (*vide* Fig. 5). Specifically, the Ce_{0.95}Cu_{0.05} sample exhibits the most remarkable catalytic activity ($r_{\text{CO}} = 6.76 \text{ mmol}_{\text{CO}} \text{ m}^{-2} \text{ h}^{-1}$) and a CO conversion of 50% already occurred at 162 °C. The Ce_{0.95}Mn_{0.025}Cu_{0.025} catalyst has a slightly

lower catalytic activity ($r_{\text{CO}} = 4.59 \text{ mmol}_{\text{CO}} \text{ m}^{-2} \text{ h}^{-1}$), whereas the Ce_{0.95}Mn_{0.05} is evidently less active than both the Cu-containing catalysts ($r_{\text{CO}} = 1.66 \text{ mmol}_{\text{CO}} \text{ m}^{-2} \text{ h}^{-1}$). Finally, the least performing catalyst is the CeO₂ ($r_{\text{CO}} = 1.30 \text{ mmol}_{\text{CO}} \text{ m}^{-2} \text{ h}^{-1}$). Therefore, the specific reaction rates follow the increasing order:

$$\text{CeO}_2 < \text{Ce}_{0.95}\text{Mn}_{0.05} < \text{Ce}_{0.95}\text{Mn}_{0.025}\text{Cu}_{0.025} < \text{Ce}_{0.95}\text{Cu}_{0.05}$$

The rates for the aerobic CO oxidation reaction over doped-ceria catalysts are more discriminable from each other than those derived from the CO-TPR analysis. It seems, indeed, that in the absence of gas-phase oxygen, the oxidation activity depends on the lattice oxygens, whereas for the CO oxidation reaction under aerobic condition both the surface and lattice oxygens play a role. It appears that the surface defects evaluated by the Raman spectroscopy (*vide supra*) promotes the CO oxidation activity under either anaerobic and aerobic conditions. In fact, a positive correlation can be observed between the $O_{\text{v}}/F_{2\text{g}}$ and the r_{CO} values (Tables 3, 4, respectively). This correlation is higher for the CO oxidation reaction under anaerobic conditions (CO-TPR analysis). In order to evaluate the stability of the prepared samples, several test–retest cycles have been performed (data not reported for the sake of brevity). As shown in Fig. 8, the most performing catalyst (Ce_{0.95}Cu_{0.05}) provided a good stability for two successive runs up to 700 °C. Catalytic activities of the fresh and aged sample (the latter was obtained by heating the powder at 700 °C for 8 h) are comparable, thus suggesting a good stability of the catalyst.

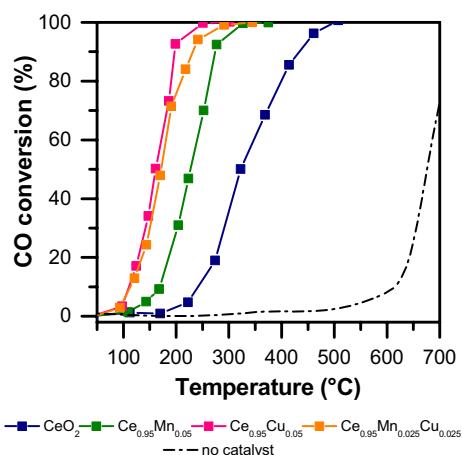


Fig. 7 CO conversion (%) as a function of temperature over the prepared catalysts

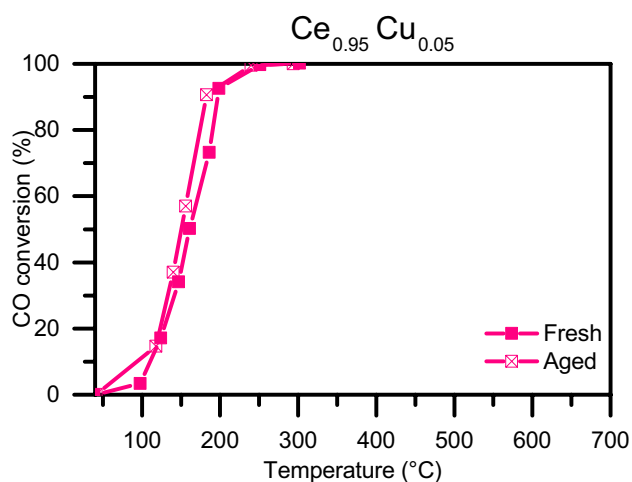
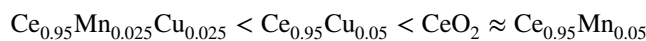


Fig. 8 CO conversion (%) over the sample $\text{Ce}_{0.95}\text{Cu}_{0.05}$: a comparison between the fresh and the aged sample

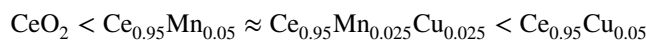
3.4.2 Soot Oxidation

Figure 9 shows the profiles of soot conversion and CO_x evolution achieved over the catalysts during the soot oxidation reaction. Table 4 also summarises two performance parameters, $T_{\text{conv}(\%)}$ ($^{\circ}\text{C}$) and r_{soot} ($\text{mmol}_{\text{soot}} \text{g}_{\text{cat}}^{-1} \text{h}^{-1}$). The latter is defined as the rate of disappearance of soot normalised with respect to the catalyst weight at a certain temperature (320 $^{\circ}\text{C}$ was selected as the reference).

From the soot conversion profiles, it can be noticed that the soot oxidation values appear higher for the $\text{Ce}_{0.95}\text{Mn}_{0.05}$ and CeO_2 samples rather than for the $\text{Ce}_{0.95}\text{Cu}_{0.05}$ and $\text{Ce}_{0.95}\text{Mn}_{0.025}\text{Cu}_{0.025}$. The well-defined nanocubic structure that constitutes CeO_2 apparently still plays the key role in soot oxidation, thanks to its highly reactive low-index surfaces, even if the presence of dopants promotes the reaction. Therefore, the following conversion trend appears:



It is also worth noticing that this activity trend correlates with the Soot-TPR profiles above 400 $^{\circ}\text{C}$ (in terms of CO_2 production). This suggests that a high catalytic activity towards the soot oxidation takes place by a good lattice-to-surface oxygen mobility. On the other hand, a different trend is observed for the specific rates calculated at 320 $^{\circ}\text{C}$ (data in Table 4). Indeed, the following order can be drawn:



This finding is probably due to the higher surface areas for both the Cu-containing samples. At low temperatures, indeed, surface oxygens may play a major role on the oxidation activity. Figure 9 also shows the profiles of CO_2 and CO as a function of temperature during the soot oxidation. Then, the presence of the solid catalyst not only lowers the reaction temperature but also enhances the selectivity to CO_2 . Finally, Fig. 10 shows two successive catalytic cycles (up to 650 $^{\circ}\text{C}$) for the fresh and aged $\text{Ce}_{0.95}\text{Mn}_{0.05}$ sample, the “most effective” catalyst for this reaction. The latter exhibits a very good stability in terms of soot conversion and CO_x selectivity.

4 Conclusions

In the present work, a set of ceria-based catalysts doped with Mn and Cu was synthesised via a hydrothermal method. The prepared catalysts were characterized by nanocubes in the case of CeO_2 and by nanopolyhedra for binary ($\text{Ce}_{0.95}\text{Mn}_{0.05}$, $\text{Ce}_{0.95}\text{Cu}_{0.05}$) and ternary oxides ($\text{Ce}_{0.95}\text{Mn}_{0.025}\text{Cu}_{0.025}$).

The CO-TPR analysis has confirmed that the low-temperature reducibility follows the order: $\text{CeO}_2 < \text{Ce}_{0.95}\text{Mn}_{0.05} < \text{Ce}_{0.95}\text{Mn}_{0.025}\text{Cu}_{0.025} < \text{Ce}_{0.95}\text{Cu}_{0.05}$. A similar trend has also been encountered for the surface defective sites, analysed via the Raman spectroscopy. These findings confirm

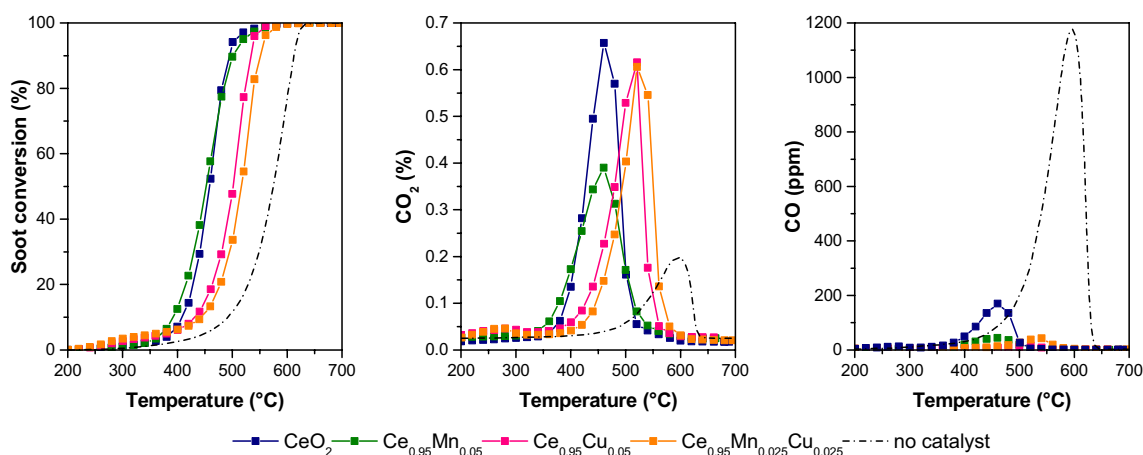


Fig. 9 Soot conversion, CO and CO_2 concentration as a function of temperature during the soot oxidation tests

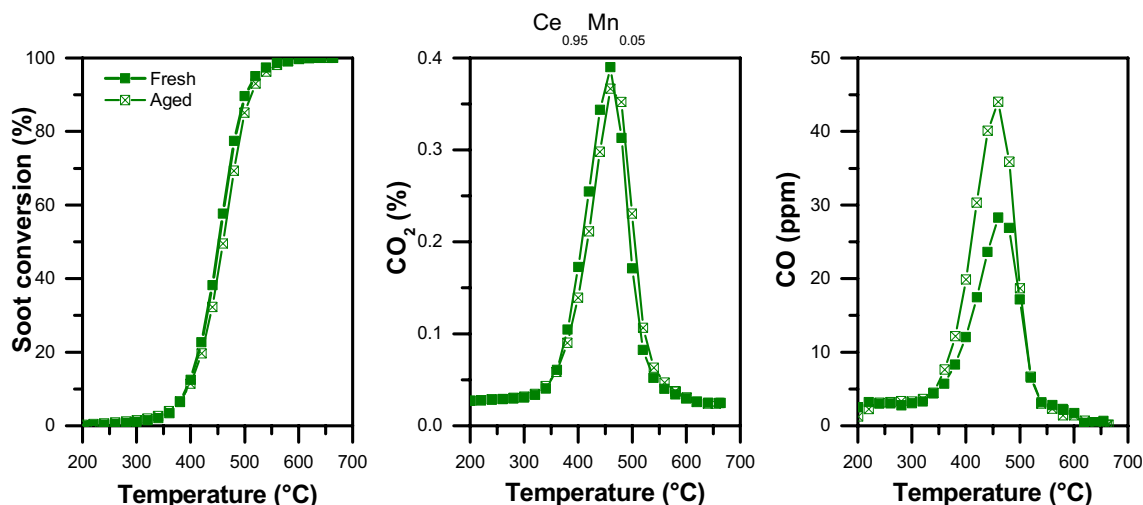


Fig. 10 Soot oxidation over the Ce_{0.95}Mn_{0.05} sample: comparison between the fresh and aged sample

the beneficial role of dopants (Mn, Cu) into the CeO₂ framework, since both the structural defects and the surface reducibility improve. Then, both the properties promote the CO oxidation activity. In fact, the Ce_{0.95}Cu_{0.05} was the most effective catalyst for the CO oxidation reaction.

On the other hand, the Ce_{0.95}Mn_{0.05} sample exhibited the best performances (in terms of overall soot conversion) for the soot oxidation. The following order was achieved: Ce_{0.95}Mn_{0.025}Cu_{0.025} < Ce_{0.95}Cu_{0.05} < CeO₂ ≈ Ce_{0.95}Mn_{0.05}, which is in agreement with the reduction profiles obtained by the Soot-TPR above 400 °C.

References

- Andana T, Piumetti M, Bensaid S, Veyre L, Thieuleux C, Russo N, Fino D, Quadrelli EA, Pirone R (2017) Ceria-supported small Pt and Pt 3 Sn nanoparticles for NO_x-assisted soot oxidation. *Appl Catal B* 209:295–310. doi:10.1016/j.apcatb.2017.03.010
- Piumetti M, Bensaid S, Russo N, Fino D (2015) Nanostructured ceria-based catalysts for soot combustion: Investigations on the surface sensitivity. *Appl Catal B* 165:742–751. doi:10.1016/j.apcatb.2014.10.062
- Setiabudi A, Chen J, Mul G, Makkee M, Moulijn JA (2004) CeO₂ catalysed soot oxidation: The role of active oxygen to accelerate the oxidation conversion. *Appl Catal B* 51:9–19. doi:10.1016/j.apcatb.2004.01.005
- Bueno-López A (2014) Diesel soot combustion ceria catalysts. *Appl Catal B* 146:1–11. doi:10.1016/j.apcatb.2013.02.033
- Arena F, Di Chio R, Fazio B, Espro C, Spiccia L, Palella A, Spadaro L (2017) Probing the functionality of nanostructured MnCeO_x catalysts in the carbon monoxide oxidation: part I. Influence of cerium addition on structure and CO oxidation activity. *Appl Catal B* 210:14–22. doi:10.1016/j.apcatb.2017.03.049
- Aneggi E, Llorca J, Boaro M, Trovarelli A (2005) Surface-structure sensitivity of CO oxidation over polycrystalline ceria powders. *J Catal* 234:88–95. doi:10.1016/j.jcat.2005.06.008
- Aneggi E, Wiater D, de Leitenburg C, Llorca J, Trovarelli A (2014) Shape-dependent activity of ceria in soot combustion. *ACS Catal* 4:172–181. doi:10.1021/cs400850r
- Trovarelli A (1996) Catalytic properties of ceria and CeO₂-containing materials. *Catal Rev* 38:439–520. doi:10.1080/01614949608006464
- Di Monte R, Kašpar J (2004) On the role of oxygen storage in three-way catalysis. *Top Catal* 28:47–57. doi:10.1023/B:TOCA.0000024333.08447.f7
- Doornkamp C, Ponc V (2000) The universal character of the Mars and Van Krevelen mechanism. *J Mol Catal A* 162:19–32. doi:10.1016/S1381-1169(00)00319-8
- Gupta A, Waghmare UV, Hegde MS (2010) Correlation of oxygen storage capacity and structural distortion in transition-metal-, noble-metal-, and rare-earth-ion-substituted CeO₂ from first principles calculation. *Chem Mater* 22:5184–5198. doi:10.1021/cm101145d
- Yuan Q, Duan H-H, Li L-L, Sun L-D, Zhang Y-W, Yan C-H (2009) Controlled synthesis and assembly of ceria-based nanomaterials. *J Colloid Interface Sci* 335:151–167. doi:10.1016/j.jcis.2009.04.007
- Vilé G, Colussi S, Krumeich F, Trovarelli A, Pérez-Ramírez J (2014) Opposite face sensitivity of CeO₂ in hydrogenation and oxidation catalysis. *Angew Chem Int Ed* 53:12069–12072. doi:10.1002/anie.201406637
- He H, Yang P, Li J, Shi R, Chen L, Zhang A, Zhu Y (2016) Controllable synthesis, characterization, and CO oxidation activity of CeO₂ nanostructures with various morphologies. *Ceram Int* 42:7810–7818. doi:10.1016/j.ceramint.2016.02.005
- Yang Z, Zhou K, Liu X, Tian Q, Lu D, Yang S (2007) Single-crystalline ceria nanocubes: size-controlled synthesis, characterization and redox property. *Nanotechnology* 18:185606. doi:10.1088/0957-4484/18/18/185606
- Mai H-X, Sun L-D, Zhang Y-W, Si R, Feng W, Zhang H-P, Liu H.-C.L. Yan C-H (2005) Shape-selective synthesis and oxygen storage behavior of ceria nanopolyhedra, nanorods, and nanocubes. *J Phys Chem B*. doi:10.1021/JP055584B
- Piumetti M, Andana T, Bensaid S, Russo N, Fino D, Pirone R (2016) Study on the CO oxidation over ceria-based nanocatalysts. *Nanoscale Res Lett* 11:165. doi:10.1186/s11671-016-1375-z
- Andana T, Piumetti M, Bensaid S, Russo N, Fino D, Pirone R (2016) Nanostructured ceria-praseodymia catalysts for diesel

- soot combustion. *Appl Catal B* 197:125–137. doi:[10.1016/j.apcatb.2015.12.030](https://doi.org/10.1016/j.apcatb.2015.12.030)
19. Sayle T.X.T, Cantoni M, Bhatta UM, Parker SC, Hall SR, Möbus G, Molinari M, Reid D, Seal S, Sayle DC (2012) Strain and architecture-tuned reactivity in ceria nanostructures; enhanced catalytic oxidation of CO to CO₂. *Chem Mater* 24:1811–1821. doi:[10.1021/cm3003436](https://doi.org/10.1021/cm3003436)
 20. Nolan M, Parker SC, Watson GW (2005) The electronic structure of oxygen vacancy defects at the low index surfaces of ceria. *Surf Sci* 595:223–232. doi:[10.1016/j.susc.2005.08.015](https://doi.org/10.1016/j.susc.2005.08.015)
 21. Piumetti M, Bensaid S, Russo N, Fino D (2016) Investigations into nanostructured ceria–zirconia catalysts for soot combustion. *Appl Catal B* 180:271–282. doi:[10.1016/j.apcatb.2015.06.018](https://doi.org/10.1016/j.apcatb.2015.06.018)
 22. Krishna K, Bueno-López A, Makkee M, Moulijn JA (2007) Potential rare-earth modified CeO₂ catalysts for soot oxidation: Part III. Effect of dopant loading and calcination temperature on catalytic activity with O₂ and NO + O₂. *Appl Catal B* 75:210–220. doi:[10.1016/j.apcatb.2007.04.009](https://doi.org/10.1016/j.apcatb.2007.04.009)
 23. Rao KN, Venkataswamy P, Reddy BM (2011) Structural characterization and catalytic evaluation of supported copper–ceria catalysts for soot oxidation. *Ind Eng Chem Res* 50:11960–11969. doi:[10.1021/ie201474p](https://doi.org/10.1021/ie201474p)
 24. Konsolakis M (2016) The role of copper–ceria interactions in catalysis science: recent theoretical and experimental advances. *Appl Catal B* 198:49–66. doi:[10.1016/j.apcatb.2016.05.037](https://doi.org/10.1016/j.apcatb.2016.05.037)
 25. Atribak I, López-Suárez FE, Bueno-López A, García-García A (2011) New insights into the performance of ceria-zirconia mixed oxides as soot combustion catalysts. Identification of the role of “active oxygen” production. *Catal Today* 176:404–408. doi:[10.1016/j.cattod.2010.11.023](https://doi.org/10.1016/j.cattod.2010.11.023)
 26. Piumetti M, Bensaid S, Andana T, Russo N, Pirone R, Fino D (2017) Cerium-copper oxides prepared by solution combustion synthesis for total oxidation reactions: from powder catalysts to structured reactors. *Appl Catal B* 205:455–468. doi:[10.1016/j.apcatb.2016.12.054](https://doi.org/10.1016/j.apcatb.2016.12.054)
 27. Zheng X, Zhang X, Wang X, Wang S, Wu S (2005) Preparation and characterization of CuO/CeO₂ catalysts and their applications in low-temperature CO oxidation. *Appl Catal A* 295:142–149. doi:[10.1016/j.apcata.2005.07.048](https://doi.org/10.1016/j.apcata.2005.07.048)
 28. Liu W, Flytzani-Stephanopoulos M (1995) Total oxidation of carbon monoxide and methane over transition metal fluorite oxide composite catalysts: I. Catalyst composition and activity. *J Catal* 153:304–316. doi:[10.1006/jcat.1995.1132](https://doi.org/10.1006/jcat.1995.1132)
 29. Sudarsanam P, Hillary B, Mallesham B, Rao BG, Amin MH, Nafady A, Alsalmeh AM, Reddy BM, Bhargava SK (2016) Designing CuO_x nanoparticle-decorated CeO₂ nanocubes for catalytic soot oxidation: role of the nanointerface in the catalytic performance of heterostructured nanomaterials. *Langmuir*. doi:[10.1021/acs.langmuir.5b04590](https://doi.org/10.1021/acs.langmuir.5b04590)
 30. Tang X, Zhang B, Li Y, Xu Y, Xin Q, Shen W (2005) CuO/CeO₂ catalysts: redox features and catalytic behaviors. *Appl Catal A Gen* 288:116–125. doi:[10.1016/j.apcata.2005.04.024](https://doi.org/10.1016/j.apcata.2005.04.024)
 31. Konsolakis M (2015) Recent advances on nitrous oxide (N₂O) decomposition over non-noble-metal oxide catalysts: catalytic performance, mechanistic considerations, and surface chemistry aspects. *ACS Catal* 5:6397–6421. doi:[10.1021/acscatal.5b01605](https://doi.org/10.1021/acscatal.5b01605)
 32. Venkataswamy P, Rao KN, Jampaiah D, Reddy BM (2015) Nanostructured manganese doped ceria solid solutions for CO oxidation at lower temperatures. *Appl Catal B* 162:122–132. doi:[10.1016/j.apcatb.2014.06.038](https://doi.org/10.1016/j.apcatb.2014.06.038)
 33. Liang Y, Huang Y, Zhang H, Lan L, Zhao M, Gong M, Chen Y, Wang J (2017) Interactional effect of cerium and manganese on NO catalytic oxidation. *Environ Sci Pollut Res* 9314–9324. doi:[10.1007/s11356-017-8645-x](https://doi.org/10.1007/s11356-017-8645-x)
 34. Tikhomirov K, Kröcher O, Elsener M, Wokaun A (2006) MnOx-CeO₂ mixed oxides for the low-temperature oxidation of diesel soot. *Appl Catal B* 64:72–78. doi:[10.1016/j.apcatb.2005.11.003](https://doi.org/10.1016/j.apcatb.2005.11.003)
 35. Rani R, Prasad R (2014) Studies of carbon monoxide oxidation at ambient conditions. *Recent Res Sci Technol* 6:89–92
 36. Lu H, Kong X, Huang H, Zhou Y, Chen Y (2015) Cu–Mn–Ce ternary mixed-oxide catalysts for catalytic combustion of toluene. *J Environ Sci* 32:102–107. doi:[10.1016/j.jes.2014.11.015](https://doi.org/10.1016/j.jes.2014.11.015)
 37. Zhao F, Gong M, Zhang G, Li J (2015) Effect of the loading content of CuO on the activity and structure of CuO/Ce–Mn–O catalysts for CO oxidation. *J Rare Earths* 33:604–610. doi:[10.1016/S1002-0721\(14\)60460-9](https://doi.org/10.1016/S1002-0721(14)60460-9)
 38. Shannon RD (1976) Revised effective ionic radii and systematic studies of interatomic distances in halides and chalcogenides. *Acta Crystallogr Sect A* 32:751–767. doi:[10.1107/S0567739476001551](https://doi.org/10.1107/S0567739476001551)
 39. Konsolakis M, Carabineiro SAC, Marnellos GE, Asad MF, Soares OSGP, Pereira MFR, Órfão JJM, Figueiredo JL (2017) Volatile organic compounds abatement over copper-based catalysts: Effect of support. *Inorg Chim Acta* 455:473–482. doi:[10.1016/j.ica.2016.07.059](https://doi.org/10.1016/j.ica.2016.07.059)
 40. Andana T, Piumetti M, Bensaid S, Russo N, Fino D, Pirone R (2016) CO and soot oxidation over Ce–Zr–Pr oxide catalysts. *Nanoscale Res Lett* 11:278. doi:[10.1186/s11671-016-1494-6](https://doi.org/10.1186/s11671-016-1494-6)
 41. Soler L, Casanovas A, Escudero C, Pérez-Dieste V, Aneggi E, Trovarelli A, Llorca J (2016) Ambient pressure photoemission spectroscopy reveals the mechanism of carbon soot oxidation in ceria-based catalysts. *ChemCatChem* 8:2748–2751. doi:[10.1002/cctc.201600615](https://doi.org/10.1002/cctc.201600615)
 42. Piumetti M, Andana T, Bensaid S, Fino D, Russo N, Pirone R (2016) Ceria-based nanomaterials as catalysts for CO oxidation and soot combustion: Effect of Zr–Pr doping and structural properties on the catalytic activity. *AIChE J*. doi:[10.1002/aic.15548](https://doi.org/10.1002/aic.15548)
 43. Chen H-T, Chang J-G, Chen H-L, Ju S-P (2009) Identifying the O₂ diffusion and reduction mechanisms on CeO₂ electrolyte in solid oxide fuel cells: A DFT + U study. *J Comput Chem* 30:2433–2442. doi:[10.1002/jcc.21247](https://doi.org/10.1002/jcc.21247)
 44. Choi YM, Abernathy H, Chen H-T, Lin MC, Liu M (2006) Characterization of O₂–CeO₂ interactions using in situ Raman spectroscopy and first-principle calculations. *ChemPhysChem* 7:1957–1963. doi:[10.1002/cphc.200600190](https://doi.org/10.1002/cphc.200600190)
 45. Amadine O, Essamlali Y, Fihri A, Larzek M, Zahouily M (2017) Effect of calcination temperature on the structure and catalytic performance of copper–ceria mixed oxide catalysts in phenol hydroxylation. *RSC Adv* 7:12586–12597. doi:[10.1039/C7RA00734E](https://doi.org/10.1039/C7RA00734E)
 46. Yang C, Yu X, Heißler S, Nefedov A, Colussi S, Llorca J, Trovarelli A, Wang Y, Wöll C (2017) Surface faceting and reconstruction of ceria nanoparticles. *Angew Chemie Int Ed* 56:375–379. doi:[10.1002/anie.201609179](https://doi.org/10.1002/anie.201609179)
 47. Chen S, Li L, Hu W, Huang X, Li Q, Xu Y, Zuo Y, Li G (2015) Anchoring high-concentration oxygen vacancies at interfaces of CeO_{2-x}/Cu toward enhanced activity for preferential CO oxidation. *ACS Appl Mater Interfaces* 7:22999–23007. doi:[10.1021/acsami.5b06302](https://doi.org/10.1021/acsami.5b06302)
 48. Paunović N, Dohčević-Mitrović Z, Scurtu R, Aškračić S, Prekajski M, Matović B, Popović ZV (2012) Suppression of inherent ferromagnetism in Pr-doped CeO₂ nanocrystals. *Nanoscale* 4:5469. doi:[10.1039/c2nr30799e](https://doi.org/10.1039/c2nr30799e)
 49. Filtschew A, Hofmann K, Hess C (2016) Ceria and its defect structure: new insights from a combined spectroscopic approach. *J Phys Chem C* 120:6694–6703. doi:[10.1021/acs.jpcc.6b00959](https://doi.org/10.1021/acs.jpcc.6b00959)
 50. Spanier JE, Robinson RD, Zhang F, Chan S-W, Herman IP (2001) Size-dependent properties of CeO_{2-y} nanoparticles as studied by Raman scattering. *Phys Rev B* 64:245407. doi:[10.1103/PhysRevB.64.245407](https://doi.org/10.1103/PhysRevB.64.245407)

51. Wu Z, Li M, Howe J, Meyer HM III, Overbury SH (2010) Probing defect sites on CeO₂ nanocrystals with well-defined surface planes by Raman spectroscopy and O₂ adsorption. *Langmuir* 26:16595–16606. doi:[10.1021/la101723w](https://doi.org/10.1021/la101723w)
52. Agarwal S, Zhu X, Hensen EJM, Lefferts L, Mojet BL (2014) Defect chemistry of ceria nanorods. *J Phys Chem C* 118:4131–4142. doi:[10.1021/jp409989y](https://doi.org/10.1021/jp409989y)
53. Dohcevic-Mitrovic ZD, Grujic-Drojin M, Scepanovic M, Popovic ZV, Boskovic S, Matovic B, Zinkevich M, Aldinger F (2006) Ce_{1-x}Y(Nd)_xO_{2-δ} nanopowders: potential materials for intermediate temperature solid oxide fuel cells. *J Phys Condens Matter* 18:S2061–S2068. doi:[10.1088/0953-8984/18/33/S22](https://doi.org/10.1088/0953-8984/18/33/S22)
54. Nakajima A, Yoshihara A, Ishigame M (1994) Defect-induced Raman spectra in doped CeO₂. *Phys Rev B* 50:13297–13307. doi:[10.1103/PhysRevB.50.13297](https://doi.org/10.1103/PhysRevB.50.13297)